IEEE Access
Multidisciplinary ⋮ Rapid Review ⋮ Open Access Journal

Received 11 August 2024, accepted 19 August 2024, date of publication 23 August 2024, date of current version 2 September 2024.

Digital Object Identifier 10.1109/ACCESS.2024.3448450

RESEARCH ARTICLE

Joint Non-Local Statistical and Wavelet Tight Frame Information-Based ℓ_0 Regularization Model for Image Deblurring

YONGQUN TAN[1], LINGLI ZHANG[2,3], AND YU CHEN[1]

[1]School of Mathematics and Statistics, Chongqing Jiaotong University, Chongqing 400074, China
[2]Chongqing Key Laboratory of Statistical Optimization and Complex Data, Chongqing University of Arts and Sciences, Chongqing 402160, China
[3]Chongqing Key Laboratory of Group and Graph Theories and Applications, Chongqing University of Arts and Sciences, Chongqing 402160, China

Corresponding author: Lingli Zhang (evralingli@yeah.net)

This work was supported in part by the National Natural Science Foundation of China under Grant 62101082, in part by Chongqing Natural Science Foundation Innovation and Development Joint Fund under Grant CSTB2023NSCQ-LZX0101, in part by the Postdoctoral Fund of Natural Science Foundation of Chongqing Municipal Science and Technology Commission under Grant cstc2021jcyj-bshX0134, in part by the Science and Technology Research Program of Chongqing Municipal Education Commission under Grant KJQN202301346 and Grant KJZD-M202301303, and in part by the Natural Science Foundation Project of Yongchuan District of Chongqing under Grant 2022yc-jckx20029.

ABSTRACT The task of image deblurring is a complex and ill-posed inverse problem, which endeavors to restore a high-fidelity image from its degraded and blurred counterpart. Traditional deblurring methodologies are often confronted with the challenge of maintaining the integrity of image details and edges throughout the restoration procedure. This paper delves into an innovative approach that synergistically harnesses the power of non-local statistical properties and wavelet tight frame based ℓ_0 regularization. The presented model integrates non-local statistical priors pertaining to the image in question into its regularization framework. Meanwhile, it leverages the robustness of wavelet tight frames to counteract the inherent ill-posedness of image deblurring scenarios. This dual strategy results in a more effective preservation of fine details and edges during the deblurring process. Empirical numerical simulations corroborate the efficacy of the presented algorithm. It demonstrates a marked superiority over existing deblurring techniques in terms of quantitative metrics such as Peak Signal-to-Noise Ratio (PSNR), Root Mean Square Error (RMSE), Structural Similarity Index (SSIM), and Universal Image Quality Index (UQI). Consequently, the presented algorithm yields images of enhanced deblurring quality, substantiating its potential in image restoration.

INDEX TERMS Image deblurring, wavelet tight frame, non-local statistical information, ℓ_0 regularization.

I. INTRODUCTION

Image deblurring is a quintessential challenge within the domain of image processing, dedicated to the enhancement of image clarity by mitigating the effects of blur. This task is frequently conceptualized as an ill-posed inverse problem, which underscores the complexity and the need for sophisticated methodologies to address it. It stands as a paradigmatic issue in the realm of image restoration, garnering extensive scholarly attention and research endeavors over the past several decades, as evidenced by a plethora of academic contributions [1], [2], [3], [4], [5]. The endeavor of image deblurring is characterized by its status as an ill-conditioned linear inverse problem [6]. It entails the reconstruction of the original image x from its degraded, blurred manifestation y. The degradation process is encapsulated within a mathematical model that delineates the relationship between the original and the degraded images, typically expressed in the following form:

$$y = Ax + n. \tag{1}$$

where x is the image to be restored, y is the degraded image, A is an irreversible linear degradation matrix, and n is usually an additive Gaussian white noise. Image

The associate editor coordinating the review of this manuscript and approving it for publication was Larbi Boubchir.

restoration encompasses a spectrum of techniques, including but not limited to image deblurring, image inpainting, image denoising, super-resolution enhancement, and compressive sensing. These methodologies are designed to address various forms of image degradation, which can be modeled by distinct linear degradation matrices such as those representing blurring, downsampling, and noise. The selection of an appropriate degradation matrix is contingent upon the specific application and the nature of the image degradation in question. In the context of image deblurring, where the degradation operator A is a blurring kernel, the restoration task involves the reconstruction of the original, unblurred image x from the observed, blurred image y [1], [2], [3], [4], [5], [7]. Specifically, when the degradation operator A is an identity matrix, the problem simplifies to image denoising, where the goal is to remove noise from the image [8], [9]. In the case of image inpainting, the degradation matrix A is often a diagonal mask with binary elements, selectively preserving or nullifying pixel values at specific locations, thereby enabling the reconstruction of missing or damaged parts of the image [10], [11]. Compressive sensing, on the other hand, involves a random projection matrix A that facilitates the reconstruction of sparse signals from a limited number of measurements [12], [13]. Furthermore, when the degradation process is a combination of blurring and downsampling, the image restoration challenge is known as super-resolution, where the objective is to enhance the resolution of the image beyond the capabilities of the original acquisition system [14], [15]. This paper primarily focuses on the problem of image deblurring, exploring advanced methodologies to effectively reverse the blurring effect and recover high-quality images.

To tackle the image deblurring degradation model denoted by equation (1), it is imperative to incorporate image-specific prior knowledge into the framework as a regularization component. This integration effectively reformulates the image deblurring challenge into the ensuing optimization problem:

$$\underset{x}{argmin}\{\frac{1}{2}\|Ax-y\|_2^2+\lambda\Phi(x)\}. \tag{2}$$

where $\frac{1}{2}\|Ax-y\|_2^2$ is a fidelity term, which can ensure that the deblurred results comply with the image blurred process and ensure the similarity between the deblurred image and the observed image. $\Phi(x)$ is a regularization term for the prior information of the image to be deblurred. Given that the image restoration endeavor is frequently characterized as an ill-posed inverse problem, the incorporation of a regularization term serves to mitigate the inherent ill-posedness, thereby facilitating the attainment of a more robust solution. The regularization parameter λ plays a pivotal role in this context, as it modulates the equilibrium between the constituent elements of the model, ensuring a balanced approach to the restoration process.

The efficacy of image deblurring is fundamentally contingent upon the judicious introduction of prior information pertaining to the image in question. As such, this prior information occupies a pivotal role within the architecture of image deblurring models and algorithms. The integration of such prior information is achieved through the medium of regularization terms. Hence, the crux of the matter lies in the adept design of efficacious regularization terms. Optimization models predicated on regularization are a prevalent approach in image deblurring, with a focus on the formulation of these terms. In the extant literature, several established optimization models have been identified, including total variation models [16], [17], [18], semi-orthogonal formulations [19], and MS models [20]. While these regularization models exhibit a degree of efficacy in preserving image edges and restoring the smooth regions of an image, they are not without their shortcomings, particularly in the realm of detail and texture preservation. Furthermore, deblurring algorithms underpinned by deep learning represent another mainstream methodology. Deep learning based deblurring algorithms have demonstrated commendable restoration capabilities [21], [22]. The combination of wavelet transforms with deep learning has been instrumental in addressing practical challenges, such as facial recognition [23], as well as the privacy and security concerns of individual internet users [24].

To enhance the preservation of details and textures in the restored image, several researchers have refined the total variation model, resulting in the emergence of various weighted total variation models [25] and non-local total variation models [26]. These models are adept at maintaining the integrity of image detail and edges. Xiong et al. [27] introduced a Joint Statistical Model (JSM) in the spatial transformation domain, which leverages both local and non-local characteristics of the image to be restored, thereby effectively mitigating the occurrence of circular artifacts. The JSM has demonstrated superior image restoration quality compared to models that solely rely on either local or non-local image features. Jung et al. [28] further enhanced the MS model, devising a non-local MS model that has been successfully applied to color image restoration tasks such as deblurring, super-resolution, and mosaic removal. Inspired by the principles of JSM and regularization techniques, this paper aims to amalgamate the strengths of both approaches to develop an optimization model for image deblurring that is grounded in a joint non-local statistical and regularization framework.

The existing regularization based optimization models are pivotal in the domain of image deblurring, where the objective and its assessment are paramount. Several studies have harnessed the power of sparse transformations within the framework of optimization models to address the image deblurring challenge [29], [30], [31], [32]. These models capitalize on the inherent sparsity or prior information of the images, assuming that they exhibit certain universal characteristics under specific sparse transformations. In the majority of these studies, the ℓ_1 regularization is employed to further mitigate noise and ameliorate the ill-posed nature of

image deblurring, offering a sparser solution than the ℓ_2 regularization. However, the ℓ_0 regularization, despite being non-convex and non-smooth with solutions that are often confined to local optima, is recognized for its superior edge preservation capabilities during the deblurring process [33], [34]. In an effort to leverage the image's prior information, various sparse transformations have been integrated into the regularization terms, encompassing gradient transformations [35], wavelet transformations [36], Fourier-curvelet transformations [37], and others. Recently, the wavelet tight frame transform has emerged as a promising approach for restoring blurred images [18], [38], [39]. Inspired by these advancements, this paper introduces a novel image deblurring model that integrates joint non-local statistical information with wavelet tight frame-based ℓ_0 regularization, which is denoted as JSWD. The contributions of this work are manifold and can be distilled into three principal aspects. Firstly, the presented model incorporates joint non-local statistical information into the regularization term, effectively amalgamating local smoothness with non-local self-similarity to ensure a more reliable and robust estimation. Secondly, the tight frame transform, being an extension of both low and high-order gradient transformations, possesses an exemplary property; the multiplication of its transposed form with itself results in an identity matrix [40]. Thirdly, the model employs both the ℓ_1 norm and the ℓ_0 quasi-norm [41] to enforce sparsity. Subsequently, the Splitting Bregman Technique (SBT) is adeptly utilized to effectively decouple the components of the presented model without compromising its convergence and stability [42], [43], [44]. This approach not only streamlines the optimization process but also enhances the overall performance of the deblurring algorithm.

The structure of this paper is delineated as follows. The initial section serves as an exposition of the research background and the significance of the problem addressed within this study. The subsequent section offers an in-depth elucidation of the relationship between the wavelet tight frame transformation and the ℓ_0 quasi-norm regularization term, alongside the image deblurring model and its attendant algorithm. The penultimate section delineates an array of numerical experiments, comparing the state-of-the-art algorithms with the model introduced in this paper for the purpose of image deblurring. To culminate, the paper presents the conclusions drawn and prospective outlooks for future research.

II. MODEL AND ALGORITHM

To address the challenge of image deblurring, this manuscript introduces a novel model that integrates joint non-local statistical and wavelet tight frame information, as delineated below:

$$\underset{x}{argmin}\{\frac{1}{2}\|Ax-y\|_2^2+\lambda R_1(x)+\beta R_2(x)\}. \tag{3}$$

where A is a matrix representing a linear degradation operator which is usually non-invertible; x indicates the image to be deblurred; y is the obtained degraded image; R_1 and R_2 represent the operators of the regularization terms; λ and β are positive regularization parameters balancing fidelity term and regularization terms. It is discernible that the model presented in equation (3) encompasses a multitude of terms, which may pose a formidable challenge when approached directly without the aid of sophisticated methodologies.

To surmount the challenges inherent in the model (3), auxiliary variables are strategically introduced to disentangle the model using SBT [44]. Extant literature suggests that SBT is characterized by rapid convergence and a modest memory footprint, making it an efficacious tool for resolving a spectrum of ℓ_1 regularization-based problems. Furthermore, SBT demonstrates an aptitude for managing optimization problems predicated on regularization. The SBT is frequently employed to address the following generic unconstrained optimization problem:

$$\underset{x\in R^N}{argmin}\{f(x)+g(Hx)\}. \tag{4}$$

where $H \in R^{M\times N}$, $f : R^N \longrightarrow R$, $g : R^M \longrightarrow R$. γ is a regularization parameter. According to the augmented Lagrangian method, the model (4) can be separated into three sub-problems shown in Table 1.

TABLE 1. Splitting bregman technique (SBT).

Input: $n=0$, choose $\gamma>0$, $w^{(0)}=0$, $x^{(0)}=0$, $z^{(0)}=0$, N_{max}, ε, $e=0$.
While ($e>\varepsilon$ or $n<N_{max}$)
$x^{(n+1)} \in \underset{x}{argmin}\{f(x)+\frac{\gamma}{2}\|Hx-z^{(n)}-w^{(n)}\|_2^2$;
$z^{(n+1)} \in \underset{z}{argmin}\{g(z)+\frac{\gamma}{2}\|Hx^{(n+1)}-z-w^{(n)}\|_2^2$;
$w^{(n+1)}=w^n-(Hx^{(n+1)}-z^{(n+1)})$;
$n \longleftarrow n+1$;
$e=\frac{\|x^{(n+1)}-x^{(n)}\|_2}{\|x^{(n+1)}\|_2}$.
End
Output: $x^{(n+1)}$.

According to the frame of SBT, the presented model (3) can be defined as:

$$f(x)=\frac{1}{2}\|Ax-y\|_2^2. \tag{5}$$

$$g(z)=g(Hx)=\lambda R_1(x)+\beta R_2(x). \tag{6}$$

where $z=\begin{bmatrix}u\\v\end{bmatrix}=Hx$, $u,v\in R^N$ and $H=\begin{bmatrix}W\\I\end{bmatrix}\in R^{2N\times N}$, wavelet tight frame transform has been introduced in the model, denoted as W, and I is identity matrix. Then the presented model (3) can be transformed into the following:

$$\underset{x,z}{argmin}\{f(x)+g(z)\}, \quad s.t. Hx=z. \tag{7}$$

Similarly, the model (7) is converted into three sub-problems by the augmented Lagrangian method. Then the

$(n+1)$th solution of x can be shown as follows:

$$x^{(n+1)} \in \underset{x}{argmin}\{\frac{1}{2}\|Ax-y\|_2^2 + \frac{\gamma}{2}\|\begin{bmatrix}W\\I\end{bmatrix}x-\begin{bmatrix}u^{(n)}\\v^{(n)}\end{bmatrix}-\begin{bmatrix}w_1^{(n)}\\w_2^{(n)}\end{bmatrix}\|_2^2\}. \quad (8)$$

where $w^{(n)} = \begin{bmatrix}w_1^{(n)}\\w_2^{(n)}\end{bmatrix} \in R^{2N}$, $w_1^{(n)}, w_2^{(n)} \in R^N$. By splitting ℓ_2 norm of the model (8), it obtains that

$$x^{(n+1)} \in \underset{x}{argmin}\{\frac{1}{2}\|Ax-y\|_2^2 + \frac{\gamma}{2}\|Wx-u^{(n)}-w_1^{(n)}\|_2^2 + \frac{\gamma}{2}\|x-v^{(n)}-w_2^{(n)}\|_2^2\}. \quad (9)$$

According to SBT [44], u and v can be addressed by the following:

$$\begin{bmatrix}u^{(n+1)}\\v^{(n+1)}\end{bmatrix} \in \underset{u,v}{argmin}\{\lambda R_1(u)+\beta R_2(v) + \frac{\gamma}{2}\|Wx^{(n+1)}-u-w_1^{(n)}\|_2^2 + \frac{\gamma}{2}\|x^{(n+1)}-v-w_2^{(n)}\|_2^2\}. \quad (10)$$

It is clear that problem (10) with respect to u and v can be decoupled, and the problem (10) is solved separately as follows:

$$u^{(n+1)} \in \underset{u}{argmin}\{\lambda R_1(u) + \frac{\gamma}{2}\|Wx^{(n+1)}-u-w_1^{(n)}\|_2^2\}. \quad (11)$$

$$v^{(n+1)} \in \underset{v}{argmin}\{\beta R_2(v) + \frac{\gamma}{2}\|x^{(n+1)}-v-w_2^{(n)}\|_2^2\}. \quad (12)$$

The Lagrangian multipliers w_1 and w_2 can be updated by

$$w^{(n+1)} = \begin{bmatrix}w_1^{(n+1)}\\w_2^{(n+1)}\end{bmatrix} = \begin{bmatrix}w_1^{(n)}\\w_2^{(n)}\end{bmatrix} - (\begin{bmatrix}W\\I\end{bmatrix}x^{(n+1)} - \begin{bmatrix}u^{(n+1)}\\v^{(n+1)}\end{bmatrix}).$$

Which can be simplified as follows:

$$w_1^{(n+1)} = w_1^{(n)} - (Wx^{(n+1)} - u^{(n+1)}). \quad (13)$$

$$w_2^{(n+1)} = w_2^{(n)} - (x^{(n+1)} - v^{(n+1)}). \quad (14)$$

In conclusion, the presented model is evolved to solve the three sub-problems about variables x, z, w by SBT, respectively. In order to address the problems (11) and (12), the proximal map $prox_\alpha(g)(x)$ [4] is utilized which can be defined as follows:

$$prox_\alpha(g)(x) \in \underset{y}{argmin}\{\frac{1}{2}\|y-x\|_2^2 + \alpha g(y)\}.$$

Subsequently, the comprehensive algorithmic flowchart is delineated within Table 2.

To clarify the observed image, the original problem (3) is approached using SBT, which is methodically divided into three distinct sub-problems. The subsequent exposition will elucidate the intricate processes involved in these three sub-problems.

TABLE 2. A complete solution flowchart of the presented deblurring model.

Input: the observed image y, the operator A, the maximum iteration N_{max} and relative iteration error ε.
Initialization: $n=0, x^{(0)}=y, u^{(0)}=v^{(0)}=w_1^{(0)}=w_2^{(0)}=0, e=0$, λ, β, γ.
While ($e>\varepsilon$ or $n<N_{max}$)
$x^{(n+1)} \in \underset{x}{argmin}\{\frac{1}{2}\|Ax-y\|_2^2+\frac{\gamma}{2}\|Wx-u^{(n)}-w_1^{(n)}\|_2^2 + \frac{\gamma}{2}\|x-v^{(n)}-w_2^{(n)}\|_2^2\}$;
$u^{(n+1)} = prox_{\lambda/\gamma}(R_1)(Wx^{(n+1)}-w_1^{(n)})$;
$v^{(n+1)} = prox_{\beta/\gamma}(R_2)(x^{(n+1)}-w_2^{(n)})$;
$w_1^{(n+1)} = w_1^{(n)} - (Wx^{(n+1)}-u^{(n+1)})$;
$w_2^{(n+1)} = w_2^{(n)} - (x^{(n+1)}-v^{(n+1)})$;
$n \longleftarrow n+1$;
$e = \frac{\|x^{(n+1)}-x^{(n)}\|_2}{\|x^{(n+1)}\|_2}$.
Output: the deblurred image $x^{(n+1)}$.

A. X SUB-PROBLEM

The sub-problem (9) includes three terms. $\frac{1}{2}\|Ax-y\|_2^2$ is the fidelity term, and its two latter terms include different information about x, the regularization parameter γ may be different which is more reasonable. Therefore, γ_1 and γ_2 are introduced. Then the problem (9) can be rewritten as follows:

$$x^{(n+1)} \in \underset{x}{argmin}\{\frac{1}{2}\|Ax-y\|_2^2 + \frac{\gamma_1}{2}\|Wx-u^{(n)}-w_1^{(n)}\|_2^2 + \frac{\gamma_2}{2}\|x-v^{(n)}-w_2^{(n)}\|_2^2\}. \quad (15)$$

Through the analysis of the objective function in (15), it can obtain that the function about x is a strictly convex quadratic function, and it can get a closed form solution, which is represented as:

$$x^{(n+1)} = [A^TA+(\gamma_1+\gamma_2)I]^{-1}[A^Ty+\gamma_1W^T(u^{(n)}+w_1^{(n)}) + \gamma_2(v^{(n)}+w_2^{(n)})]. \quad (16)$$

For image inpainting or image deblurring problem, the equation (16) can be computed efficiently and directly.

In this paper, image deblurring is considered, and A represents a circular convolution matrix which can be factorized as follows:

$$A = F^{-1}DF. \quad (17)$$

where F is the matrix which denotes 2D discrete Fourier transform, F^{-1} is its inverse and D is a diagonal matrix which is related to the Fourier transform coefficients of the convolution operator A. Thus, $[A^TA+(\gamma_1+\gamma_2)I]^{-1}$ can be expressed as

$$[A^TA+(\gamma_1+\gamma_2)I]^{-1} = [F^{-1}D^*DF+(\gamma_1+\gamma_2)F^{-1}F]^{-1} = F^{-1}[D^*D+(\gamma_1+\gamma_2)I]^{-1}F. \quad (18)$$

where * denotes complex conjugate. Since $D^*D+(\gamma_1+\gamma_2)I$ is diagonal, the cost of its inversion is O(N). Similarly, the product of F^{-1} and F can be implemented with O(NlogN) by using fast Fourier transform algorithm.

B. U SUB-PROBLEM

In the aforementioned sub-problem, the proximal mapping corresponding to $R_1(\cdot)$ [4] leverages a wavelet tight frame, which is expanded through total variation, and employs the ℓ_0 quasi-norm to more effectively mitigate the ill-posed nature of the problem, denoted as $\|Wx\|_0$. Despite the ℓ_0 regularization problem being classified as NP-hard, the hard thresholding algorithm [42] provides a viable solution to surmount this challenge. Consequently, the sub-problem for u can be articulated as follows:

$$\begin{aligned} u^{(n+1)} &= prox_{\lambda/\gamma_1}(R_1)(Wx^{(n+1)} - w_1^{(n)}) \\ &= \underset{u}{argmin}\{\frac{1}{2}\|u - (Wx^{(n+1)} - w_1^{(n)})\|_2^2 + \frac{\lambda}{\gamma_1}R_1(u)\} \\ &= \underset{u}{argmin}\{\frac{2\lambda}{\gamma_1}\|u\|_0 + \|u - (Wx^{(n+1)} - w_1^{(n)})\|_2^2\}. \end{aligned} \tag{19}$$

Utilizing the hard threshold algorithm to resolve equation (19), the algorithm yields the $(n+1)$th iteration's solution pertaining to the variable u.

$$u^{(n+1)} = \begin{cases} \{0\}, & Wx^{(n+1)} - w_1^{(n)} < \sqrt{\frac{2\lambda}{\gamma_1}}; \\ \{Wx^{(n+1)} - w_1^{(n)}\}, & Wx^{(n+1)} - w_1^{(n)} > \sqrt{\frac{2\lambda}{\gamma_1}}; \\ \{Wx^{(n+1)} - w_1^{(n)}, 0\}, & Wx^{(n+1)} - w_1^{(n)} = \sqrt{\frac{2\lambda}{\gamma_1}}. \end{cases} \tag{20}$$

C. V SUB-PROBLEM

Upon the computation of $x^{(n+1)}$ and $u^{(n+1)}$, attention is then directed towards the sub-problem concerning v. In light of the resolution of the aforementioned sub-problems for $x^{(n+1)}$ and $u^{(n+1)}$, the formulation of the v sub-problem is as follows:

$$\begin{aligned} v^{(n+1)} &= prox_{\beta/\gamma_2}(R_2)(x^{(n+1)} - w_2^{(n)}) \\ &= \underset{v}{argmin}\{\frac{1}{2}\|v - (x^{(n+1)} - w_2^{(n)})\|_2^2 + \frac{\beta}{\gamma_2}R_2(v)\} \\ &= \underset{v}{argmin}\{\frac{1}{2}\|v - (x^{(n+1)} - w_2^{(n)})\|_2^2 + \frac{\beta}{\gamma_2}\|\Phi_v\|_1\}. \end{aligned} \tag{21}$$

where Φ_v symbolizes the transformational operator applied to a module that encapsulates non-local means of the image slated for deblurring. An exhaustive elucidation of Φ_v is available within the context of the three-dimensional spatial transformation domain's self-similarity non-local statistical model, as referenced in [27].

Assuming $\beta/\gamma_2 = \eta, x^{(n+1)} - w_2^{(n)} = p^{(n)}$, the equation (21) can be rewritten as:

$$v^{(n+1)} \in \underset{v}{argmin}\{\frac{1}{2}\|v^{(n)} - p^{(n)})\|_2^2 + \eta\|\Phi_v\|_1\}. \tag{22}$$

Assuming N is the dimension of v and p, and K is the dimension of Φ_v and Φ_p, $\rho = K\eta/N$, $j = 1, .., K$, the following equation holds:

$$\frac{1}{N}\|v^{(n)} - p^{(n)})\|_2^2 = \frac{1}{K}\|\Phi_v^{(n)} - \Phi_p^{(n)}\|_2^2. \tag{23}$$

By combining equations (22) and (23), it becomes straightforward to infer that equation (21) is reformulated as follows:

$$v^{(n+1)} \in \underset{v}{argmin}\{\frac{1}{2}\|\Phi_v^{(n)} - \Phi_p^{(n)}\|_2^2 + \rho\|\Phi_v\|_1\}. \tag{24}$$

By using the soft threshold algorithm to solve (24), we can obtain $\Phi_v^{(n)}$:

$$\begin{aligned} \Phi_v^{(n)} &= sgn(\Phi_p^{(n)}(j))max\{\|\Phi_p^{(n)}(j)\| - \sqrt{2\rho}, 0\} \\ &= \begin{cases} \Phi_p^{(n)}(j) - \sqrt{2\rho}, \Phi_p^{(n)}(j) \in (\sqrt{2\rho}, +\infty); \\ 0, \Phi_p^{(n)}(j) \in (-\sqrt{2\rho}, \sqrt{2\rho}); \\ \Phi_p^{(n)}(j) + \sqrt{2\rho}, \Phi_p^{(n)}(j) \in (-\infty, -\sqrt{2\rho}). \end{cases} \end{aligned} \tag{25}$$

Then $v^{(n+1)}$ is equal to

$$\begin{aligned} v^{(n+1)} &= R_2(\Phi_v^{(n)}) \\ &= R_2(soft(\Phi_p^{(n)}, \sqrt{2\rho})) \\ &= R_2(soft(\Phi(x^{(n+1)} - w_2^{(n)}), \sqrt{2\rho})). \end{aligned} \tag{26}$$

where *soft* represents the soft threshold algorithm. A more detailed derivation process for solving the v sub-problem can be found in reference [27].

D. SUMMARY

As the presented model is not amenable to direct resolution, auxiliary variables u, v, w_1 and w_2 are introduced to facilitate its decoupling. A comprehensive flowchart delineating the algorithm is encapsulated in Table 3.

TABLE 3. A detailed flowchart description of the presented algorithm.

Input: the observed image y, the operator A, the maximum iteration N_{max}
Initialization: $n = 0$, $x^{(0)} = y$, $u^{(0)} = v^{(0)} = w_1^{(0)} = w_2^{(0)} = 0$, λ, β, γ_1, γ_2.
While $(n < N_{max})$
Compute $x^{(n+1)}$ by (16);
Compute $u^{(n+1)}$ by (20);
Compute $v^{(n+1)}$ by (26);
$w_1^{(n+1)} = w_1^{(n)} - (Wx^{(n+1)} - u^{(n+1)})$;
$w_2^{(n+1)} = w_2^{(n)} - (x^{(n+1)} - v^{(n+1)})$;
$n \longleftarrow n + 1$;
Until the maximum number of iterations is reached.
Output: the deblurred image $x^{(n+1)}$.

III. NUMERICAL EXPERIMENTS

The numerical experiment environment of this paper was conducted on an HP laptop Intel (R) Core (TM) i5-7200U CPU @ 2.50GHz 2.71 GHz, with a RAM4.00G, 64 bit operating system, and MATLAB 2021a installed on an x64 processor.

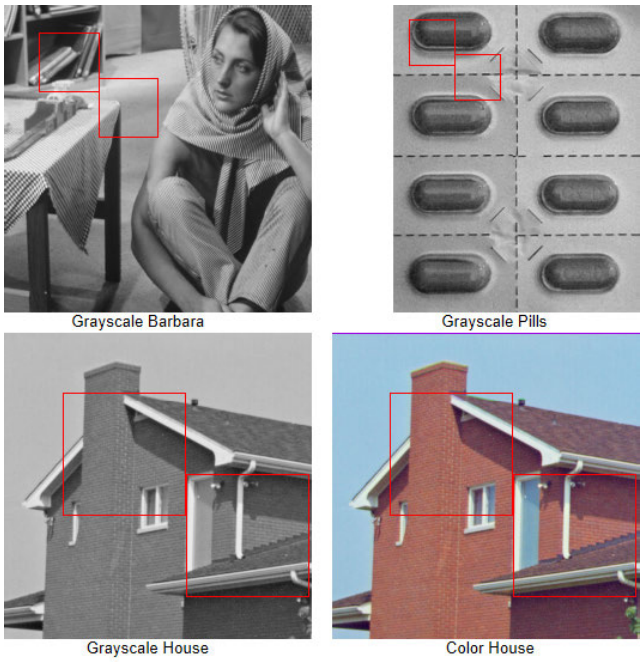

FIGURE 1. It represents the reference images including grayscale 'Barbara', grayscale 'Pills', grayscale 'House' and color 'House'.

A. SOURCE OF EXPERIMENTAL IMAGES

The experimental dataset comprises four images, depicted in Figure 1, which include the grayscale renditions of 'Barbara', 'Pills', and 'House', as well as a color version of 'House'. These images are sourced from the publication 'Digital Image Processing Using MATLAB, 2nd edition' [45]. To facilitate a comparative analysis of the efficacy of various deblurring algorithms, two distinct regions from each image have been selected and are indicated by the two red rectangular frames.

B. PARAMETER SETTING

The presented model in this paper necessitates the determination of five parameters: λ, β, γ_1, γ_2 and the number of iterations N_{max}. For the experimental parameter tuning, the initial values are set as follows: $\lambda = 3$, $\beta = 20$, $\gamma_1 = 7 \times 10^{-7}$, and $\gamma_2 = 2 \times 10^{-3}$. A series of experiments concerning the parameter configuration for image deblurring are conducted. The grayscale 'House' image, characterized by a mean blur and noise level of 25/255, is utilized for the parameter setting experiment. The iteration limit N_{max} is established at 30, and the Peak Signal-to-Noise Ratio (PSNR) is recorded. The variations in the regularization parameters and the corresponding PSNR values are presented in Table 4, revealing a maximum PSNR of 40.4309 dB and a minimum of 37.6569 dB. The experimental adjustments to the parameters have led to a notable enhancement in PSNR, amounting to an approximate improvement of 2.7740 dB.

According to the above numerical experiments, the selected parameters of the presented model are as follows: $\lambda = 2$, $\beta = 1.5$, $\gamma_1 = 7 \times 10^{-9}$, and $\gamma_2 = 1.5 \times 10^{-3}$ by trial and error. The number of iterations N_{max} is set to 100. The presented model can obtain high-quality deblurred images.

TABLE 4. Parameter Setting for the presented model.

λ	β	γ_1	γ_2	PSNR(dB)
3	20	7×10^{-7}	2×10^{-3}	37.6569
3	16	7×10^{-7}	2×10^{-3}	37.8179
3	10	7×10^{-7}	2×10^{-3}	38.2598
3	5	7×10^{-7}	2×10^{-3}	39.0483
3	2	7×10^{-7}	2×10^{-3}	39.9470
3	1	7×10^{-7}	2×10^{-3}	40.0316
3	1.5	7×10^{-7}	2×10^{-3}	40.0800
4	1.5	7×10^{-7}	2×10^{-3}	40.0800
2	1.5	7×10^{-7}	2×10^{-3}	40.0804
2	1.5	7×10^{-6}	2×10^{-3}	38.9106
2	1.5	7×10^{-8}	2×10^{-3}	40.2023
2	1.5	7×10^{-9}	2×10^{-3}	40.2120
2	1.5	7×10^{-9}	1×10^{-3}	40.3606
2	1.5	7×10^{-9}	3×10^{-3}	39.7026
2	1.5	7×10^{-9}	1.5×10^{-3}	40.4309
2	1.5	7×10^{-9}	8×10^{-4}	39.6854
2	1.5	7×10^{-9}	1.75×10^{-3}	40.3328
2	1.5	7×10^{-9}	1.6×10^{-3}	40.3955

C. EXPERIMENTAL RESULTS

The acquisition of a blurred image entails the original, high-resolution image undergoing convolution with a blurring kernel, succeeded by the superimposition of Gaussian noise characterized by a standard deviation σ. The experimental protocol incorporated three distinct blurring methodologies: mean blur, Gaussian blur, and motion blur. For the mean blur, the process commenced with the computation of the arithmetic mean across each 9×9 pixel block of the original image, followed by the incorporation of zero-mean additive Gaussian white noise with a standard deviation of 25/255. In the case of Gaussian blur, the original image was subjected to the addition of Gaussian noise with a mean of 25 and a standard deviation of 1.6, prior to the introduction of zero-mean additive Gaussian white noise with a standard deviation of 25/255. The motion blur was achieved by applying a 45-degree counterclockwise rotation and a 20-pixel translation to the photographic subject, culminating in the addition of zero-mean additive Gaussian white noise with a standard deviation of 25/255.

Within the scope of numerical experimentation, a comparative analysis of image deblurring was conducted using the algorithms referenced in [5], [7], [22], [27], and [36], which are denoted as BM3D, CBM3D, IRCNN, JSM and EDDT, respectively. The algorithm introduced in this paper is designated as JSWD.

There are four quantitative assessments to be utilized to assess the deblurring algorithms, namely Peak Signal-to-Noise Ratio (PSNR) [46], Root Mean Square Error (RMSE) [47], Structural Similarity Index (SSIM) [48], and Universal Image Quality Index (UQI) [49]. PSNR can be expressed as

$$PSNR = 10log_{10}(\frac{max^2}{MSE}). \tag{27}$$

where the unit of PSNR is decibels (dB), max is the highest scale value of the 8-bits gray scale. MSE is the root mean square error of the clear image x and the deblurred

TABLE 5. Quantitative assessments including PSNR, RMSE, SSIM and UQI are utilized for different gray image deblurring algorithms.

Image	BM3D [5]	JSM [27]
9×9 Mean Blur, $\sigma = 25/255$		
Barbara	22.42/19.28/0.71/0.93	27.16/11.17/0.91/0.97
Pills	27.04/11.33/0.84/0.96	37.59/3.36/0.96/0.99
House	24.12/15.86/0.80/0.93	37.31/3.47/0.92/0.99
Gaussian Blur: fspecial('Gaussian', 25, 1.6), $\sigma = 25/255$		
Barbara	23.48/17.07/0.76/0.94	25.97/12.81/0.92/0.97
Pills	30.20/7.87/0.89/0.98	39.70/2.63/0.99/0.99
House	27.48/10.76/0.84/0.97	35.64/4.21/0.90/0.99
Motion Blur: fspecial('motion', 20, 45), $\sigma = 25/255$		
Barbara	21.68/21.00/0.69/0.91	31.72/6.61/0.97/0.99
Pills	25.42/13.65/0.81/0.94	38.44/3.04/0.97/0.99
House	21.73/20.88/0.79/0.87	37.09/3.56/0.90/0.99
Image	EDDT [40]	JSWD
9×9 Mean Blur, $\sigma = 25/255$		
Barbara	23.77/16.51/0.80/0.95	32.92/5.75/0.97/0.99
Pills	32.20/6.25/0.87/0.98	40.34/2.45/0.98/0.99
House	29.72/8.32/0.81/0.98	40.67/2.35/0.96/0.99
Gaussian Blur: fspecial('Gaussian', 25, 1.6), $\sigma = 25/255$		
Barbara	24.50/15.18/0.85/0.95	27.33/10.95/0.95/0.97
Pills	35.09/4.48/0.93/0.99	40.94/2.28/0.99/0.99
House	32.57/5.99/0.85/0.99	37.15/3.53/0.92/0.99
Motion Blur: fspecial('motion', 20, 45), $\sigma = 25/255$		
Barbara	24.08/15.92/0.80/0.95	38.30/3.09/0.99/0.99
Pills	30.78/7.36/0.85/0.98	41.72/2.08/0.99/0.99
House	29.44/8.59/0.81/0.98	41.06/2.25/0.96/0.99

image $x^{(n+1)}$, which can be expressed as

$$MSE = \frac{\sum_{i=1}^{H}\sum_{j=1}^{W}\sum_{k=1}^{D}(x(i,j,k) - x^{(n+1)}(i,j,k))^2}{H \times W \times D}.$$

where H, W, and D represents the height, width, and dimension of the image x, respectively. $x(i,j,k)$ represents the pixel value in the i-th row, j-th column, and k-th dimension of the image x, i, j, k is the subscript index. PSNR is based on pixel value calculation, which is simple and fast, but it does not conform to the human visual system. PSNR is related to MSE, and another quantitative assessment is also related to MSE, which is RMSE, which means taking the arithmetic square root of MSE. The mathematical language of RMSE is

$$RMSE = \sqrt{\frac{\sum_{i=1}^{H}\sum_{j=1}^{W}\sum_{k=1}^{D}(x(i,j,k) - x^{(n+1)}(i,j,k))^2}{H \times W \times D}}. \quad (28)$$

A lower RMSE indicates superior algorithmic performance. SSIM is predicated on three pivotal factors: luminance, contrast, and structural information, thereby addressing the inherent limitations of PSNR. SSIM quantifies the degree of similarity between the original clear image x and its deblurred counterpart $x^{(n+1)}$, with a scale that ranges from 0 to 1, where 1 denotes perfect similarity. SSIM is defined as

$$SSIM = \frac{(2\mu_1\mu_2 + c_1)(\sigma_{12} + c_2)}{(\mu_1^2 + \mu_2^2 + c_1)(\sigma_1^2 + \sigma_2^2 + c_2)}. \quad (29)$$

UQI is a metric renowned for its computational simplicity and broad applicability across diverse image processing domains

TABLE 6. Quantitative assessments including PSNR, RMSE, SSIM and UQI are utilized for different color image deblurring algorithms.

Image	CBM3D [7]	JSM [27]
9×9 Mean Blur, $\sigma = 25/255$		
House	23.44/9.76/0.84/0.98	35.84/2.36/0.98/1.00
Gaussian Blur: ('Gaussian', 25, 1.6), $\sigma = 25/255$		
House	26.48/6.87/0.91/0.99	34.31/2.81/0.97/0.99
Motion Blur: fspecial('motion', 20, 45), $\sigma = 25/255$		
House	21.22/12.61/0.79/0.96	35.71/2.40/0.98/1.00
Image	IRCNN [22]	JSWD
9×9 Mean Blur, $\sigma = 25/255$		
House	26.33/6.91/0.91/0.99	38.87/1.66/0.99/1.00
Gaussian Blur: fspecial('Gaussian', 25, 1.6), $\sigma = 25/255$		
House	29.05/5.16/0.94/0.99	34.00/2.88/0.98/1.00
Motion Blur: fspecial('motion', 20, 45), $\sigma = 25/255$		
House	25.67/7.48/0.90/0.99	39.66/1.52/0.99/1.00

for the assessment of image fidelity [49]. It is formulated as follows:

$$UQI = \frac{4\mu_1\mu_2\sigma_{12}}{(\mu_1^2 + \mu_2^2)(\sigma_1^2 + \sigma_2^2)}. \quad (30)$$

where μ_1 is the mean of the deblurred image $x^{(n+1)}$, and μ_2 is the mean of the clear image x, σ_1 is the variance of the deblurred image $x^{(n+1)}$, and σ_2 is the variance of the clear image x, σ_{12} is the covariance between the deblurred image $x^{(n+1)}$ and the clear image x, c_1 and c_2 are constants. It is reasonable and feasible to comprehensively evaluate the quality of images using PSNR, RMSE, SSIM, and UQI in this paper.

At a noise standard deviation of $\sigma = 25/255$, to streamline the compilation of a comparative table for the numerical outcomes of quantitative metrics, the values have been taken to two decimal places. The quantitative assessments are detailed in the respective columns of Tables 5 and 6.

Table 5 encompasses quantitative assessments, including PSNR, RMSE, SSIM, and UQI, which are utilized to evaluate various grayscale image deblurring algorithms. It is observable from Table 5 that the PSNR values yielded by JSWD surpass those of the comparative algorithms. The most pronounced difference in PSNR is observed in the BM3D algorithm when deblurring the motion blur of the 'House' image, amounting to approximately 19.33 dB. Conversely, the minimal difference in PSNR is recorded in the JSM algorithm when deblurring the Gaussian blur of the 'Pills' image, which is approximately 1.24 dB. The PSNR achieved by JSWD for the deblurred 'Barbara' image under Gaussian blur conditions is 27.33 dB, which still exceeds the PSNR of the comparative algorithms. In terms of RMSE, it is evident that, for a given blur type, the RMSE of JSWD is more diminutive compared to the other comparative algorithms, with a range from 2.08 to 10.95. The SSIM of JSWD hovers around the interval of 0.92 to 0.99, and the UQI value consistently approaches 0.99. A quantitative assessment analysis indicates that JSWD demonstrates the most efficacious restoration for motion blur, with mean blur following suit. The most exemplary quantitative assessments for the deblurred 'Pills' image by JSWD under motion blur conditions are as follows: PSNR, RMSE, SSIM, and UQI are 41.72 dB, 2.08, 0.99, and 0.99, respectively.

Table 6 delineates a comprehensive set of quantitative assessments, encompassing PSNR, RMSE, SSIM and UQI, employed for the evaluation of various color image deblurring techniques. In the context of color image deblurring, the primary focus is on the 'House' image subjected to three distinct types of blur. The JSWD algorithm exhibits commendable quantitative assessment values, particularly in the restoration of motion and mean blurred images, with corresponding metrics of 39.66 dB, 1.52, 0.99, and 1 for motion blur, and 38.87 dB, 1.66, 0.99, and 1 for mean blur, respectively. When it comes to Gaussian blur, the quantitative assessments rendered by JSWD are marginally lower than those of the JSM algorithm but surpass those of both the CBM3D and IRCNN algorithms. This slight discrepancy in quantitative assessments between JSWD and JSM is attributed to the inferior performance of JSWD's second channel relative to JSM when independently deblurring each of the three color channels in the images.

The subsequent content provides a visual comparison of the deblurring outcomes of the comparative algorithms, with a focus on two locally magnified images along the principal diagonal direction. The sequence of images in each column represents the deblurred result and the two localized enlargements. Owing to spatial constraints within this document, a selection of three exemplary experimental results in grayscale image deblurring has been made, encompassing 'Barbara' under mean blur, 'Pills' under Gaussian blur, and 'House' under motion blur. Similarly, three representative experimental results in color image deblurring have been chosen, predicated on the three types of blurred color images of 'House'.

Figures 2 to 4 display the visual effects of the deblurring algorithms on 'Barbara', 'Pills', and 'House', along with their respective locally magnified images. The deblurred images by BM3D exhibit a significant presence of artifacts, with edge information failing to be adequately restored. The texture information of the headscarf in images deblurred by JSM is more pronounced than in those deblurred by EDDT. In comparison with the deblurred image by JSM, the image deblurred by JSWD presents enhanced detail and more distinct edges. The oblique corner of the book and tablecloth in the partial enlargement can be discerned in Figure 2. From Figures 3 to 4, it is evident that the deblurred images by JSWD exhibit clear texture structures and image edges for the 'Pills' and 'House' experimental images, whereas other comparative algorithms typically exhibit some degree of artifacts. BM3D's image restoration is predicated on the similarity of image blocks, which, due to weak similarity in blurred image blocks, may lead to the selection of dissimilar blocks, resulting in suboptimal restoration outcomes. EDDT relies on the regularization of varying intensities in smooth regions and edges of the image, yet struggles to differentiate between regions and edges in blurred images, potentially misidentifying noise points and edge artifacts as edges, thus leading to diminished image quality post-deblurring. JSM, which incorporates both total variation and non-local similarity in its regularization term, yields superior restoration results compared to BM3D and EDDT. The restoration efficacy of JSWD surpasses that of JSM due to the more efficacious utilization of wavelet tight frame information in image deblurring. Specifically, the wavelet tight frame information initially decomposes the blurred image across four layers, extracts the image features of each layer, and subsequently employs these features to reconstruct the image, thereby achieving the goal of restoring image edges and detailed texture information.

FIGURE 2. The sequence from left to right illustrates the original, unadulterated image, followed by the image compromised by noise and subjected to mean blurring. Subsequently, the outcomes of various deblurring algorithms, namely BM3D, JSM, EDDT, and JSWD, are presented on the test image 'Barbara'. The subsequent pair of miniature images offers a localized perspective for closer examination.

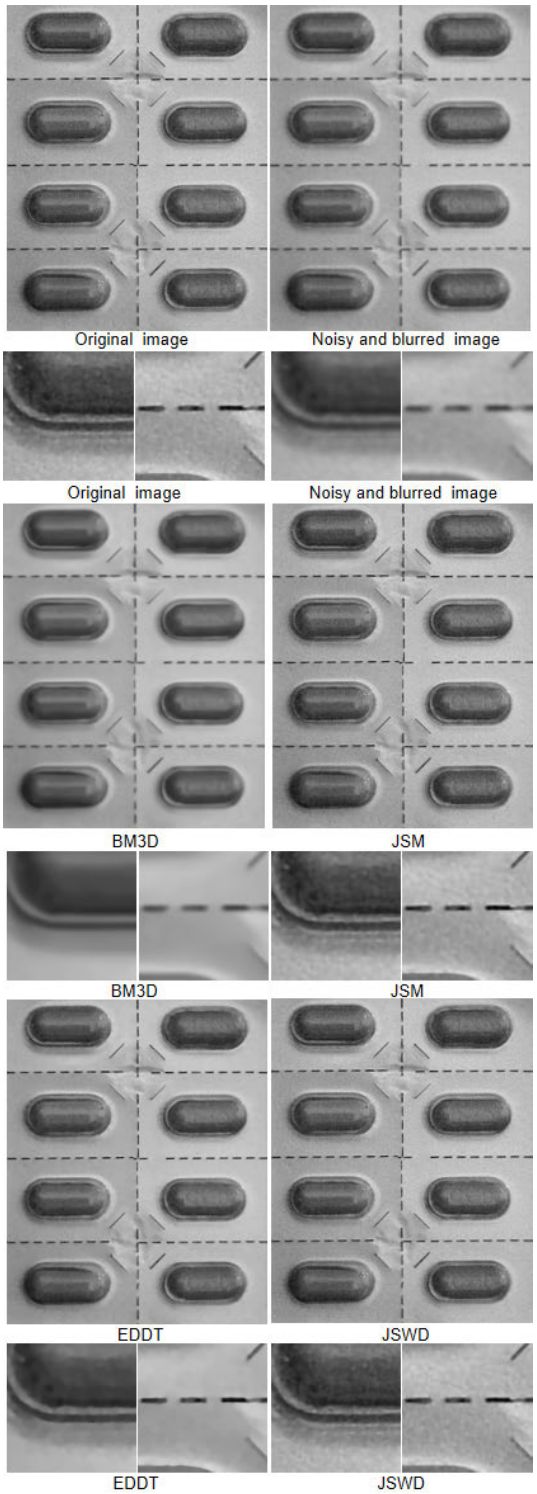

FIGURE 3. The sequence from left to right delineates the original, unaltered image, succeeded by the image that has been corrupted by noise and afflicted with Gaussian blurring. Subsequently, the deblurring outcomes of the algorithms BM3D, JSM, EDDT, and JSWD are exhibited on the test image 'Pills'. The subsequent duo of miniature images provides a localized view for a more detailed scrutiny.

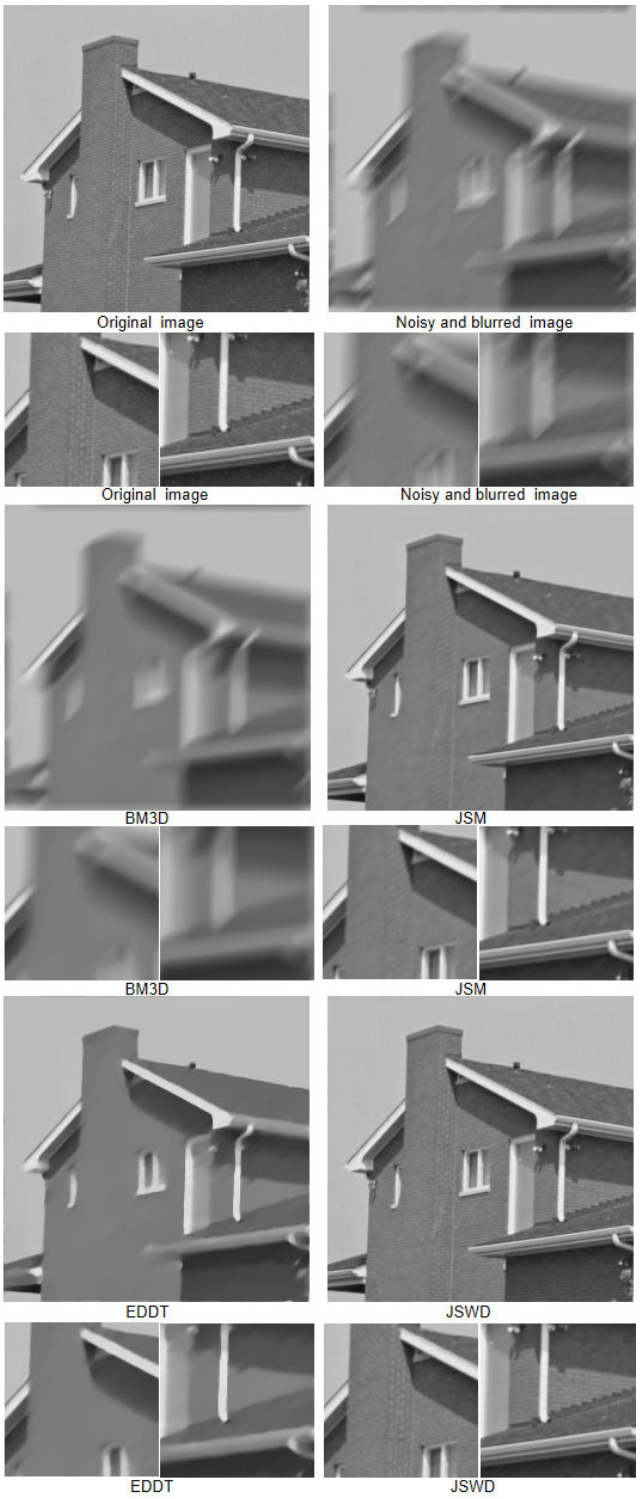

FIGURE 4. The sequence from left to right delineates the original, unaltered image, succeeded by the image that has been corrupted by noise and motion blur. Subsequently, the deblurring outcomes of the algorithms BM3D, JSM, EDDT, and JSWD are exhibited on the 'House' image. The subsequent duo of diminutive images provides a detailed, localized view for meticulous scrutiny.

Figures 5 to 7 display the visual outcomes of deblurring algorithms on three types of blurred and deblurred color images of 'House'. Consistent with the gray image experiment, the original, unadulterated image and its blurred counterpart are juxtaposed with the deblurred results yielded by various color image deblurring algorithms to facilitate an

FIGURE 5. The sequence from left to right displays the original, unaltered image, succeeded by the image that has been corrupted by noise and subjected to mean blurring. Subsequently, the deblurring results of the algorithms CBM3D, JSM, IRCNN, and JSWD are exhibited on the test image 'House'. The subsequent pair of diminutive images provide a detailed, localized view for an in-depth analysis.

FIGURE 6. The sequence from left to right displays the original, unaltered image, succeeded by a version marred by noise and Gaussian blurring. Subsequently, the deblurring outcomes of the CBM3D, JSM, IRCNN, and JSWD algorithms are delineated on the exemplar image 'House'. The subsequent pair of diminutive images provides a localized view for detailed scrutiny.

assessment of their comparative efficacy. The color image deblurring experiment employing JSWD algorithm involves the separate deblurring of the three color channels of the image. In Figure 5, the sequence from left to right represents the original clear image, the noisy and blurred image, and the deblurring outcomes of CBM3D, JSM, IRCNN,

FIGURE 7. The sequence from left to right displays the original, undistorted image, followed by the version that has been corrupted by noise and subjected to motion blurring. Subsequently, the restoration outcomes achieved through various deblurring techniques –namely, CBM3D, JSM, IRCNN and JSWD –are presented on the 'House' test color image. The subsequent pair of miniature images provides a localized perspective for detailed scrutiny.

and JSWD algorithms on the 'House' image, with the subsequent two smaller images depicting localized regions.

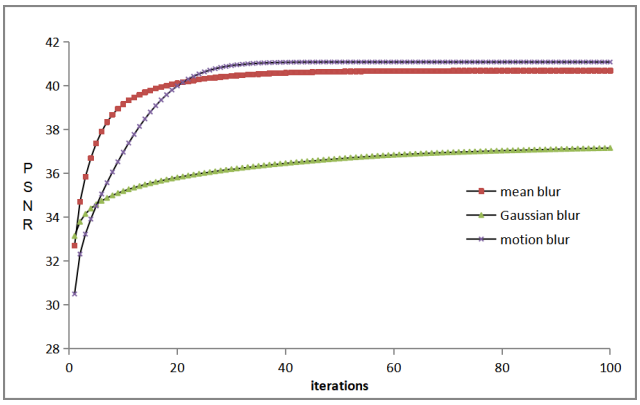

FIGURE 8. The graph illustrates the variation in PSNR as a function of the iteration count under the influence of three distinct types of image blur.

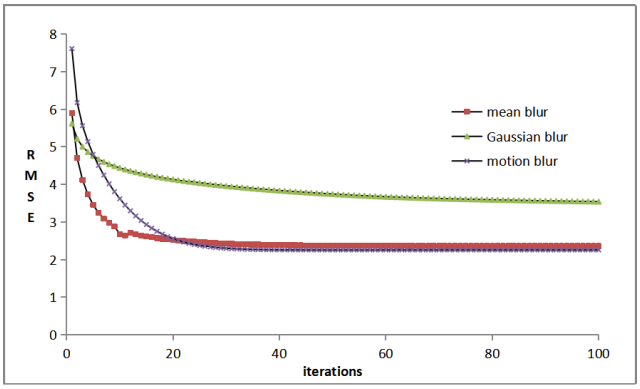

FIGURE 9. The graphical representation of RMSE as a function of iteration count is depicted for three distinct types of image blur.

Figures 5, 6, and 7 correspond to mean blur, Gaussian blur, and motion blur, respectively. The 'House' image restored by CBM3D retains a significant number of artifacts, with a slight reduction observed in Figure 6. The edge information in the images restored by IRCNN is effectively preserved, while the fine textures of the house bricks and windows are somewhat smoothed over. The image quality restored by JSM surpasses that of CBM3D and IRCNN, as evidenced by the preservation of edges in the deblurred images by JSM. The JSWD algorithm, despite a slightly lower quantitative assessment under Gaussian blur compared to JSM, delivers clearer corners in the deblurred images, particularly noticeable in the localized images.

The superior restoration outcomes achieved by the JSWD algorithm can be attributed to its sophisticated approach, which incorporates the wavelet tight frame transform alongside non-local statistical measures within the regularization term. This method adeptly harnesses both inter-group and intra-group sparsity through the concurrent application of the ℓ_0 quasi-norm and the ℓ_1 norm for regularization modeling. The synergy of these techniques endows JSWD with an enhanced capability to reconstruct images with greater fidelity, particularly in preserving edges and intricate textures that are often challenging to restore in the deblurring process.

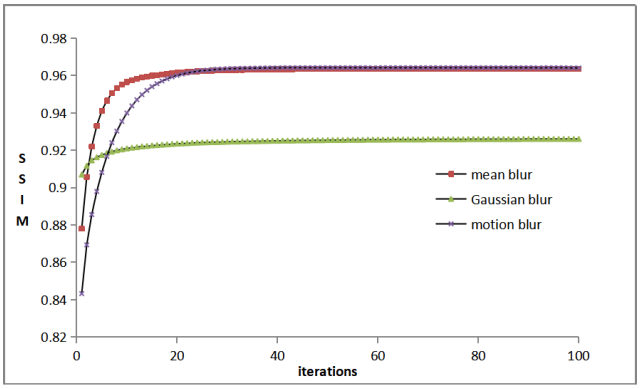

FIGURE 10. The graph of SSIM changes with the number of iterations under three kinds of blur. The graphical representation of SSIM is depicted as it fluctuates in response to varying iteration counts within the context of three distinct blurring conditions.

This multifaceted strategy not only optimizes the restoration quality but also underscores the algorithm's robustness across various types of image blurs.

D. CONVERGENCE ANALYSIS

Utilizing the grayscale image of 'House' as a benchmark, Figures 8 to 10 illustrate the fluctuation in quantitative assessments relative to the number of iterations. Initially, from 0 to 30 iterations, there is a marked variation in quantitative assessments, indicated by a steep curve. As the iterations progress from 70 to 100, the range of variation in quantitative assessments diminishes, eventually plateauing, thereby corroborating the convergence of the JSWD algorithm.

IV. CONCLUSION

In this paper, joint non-local statistical and wavelet tight frame information based ℓ_0 regularization model for image deblurring (JSWD) is presented, which integrates a dual regularization framework employing both ℓ_0 quasi-norm and ℓ_1 norm. This methodology harnesses prior knowledge of the image structure from multiple dimensions, enhancing the deblurring process. Empirical evaluations confirm that JSWD surpasses current algorithms in terms of performance and demonstrates robust convergence characteristics.

Images are ubiquitous in modern society, with high-fidelity imagery significantly enhancing visual experiences and augmenting productivity in various domains. For instance, in the medical field, crisp image edges and fine details are pivotal for clinicians to derive accurate diagnostic insights. Similarly, in vehicular applications, the clarity of images retrieved by license plate recognition systems, despite being subject to noise, is fundamental for precise plate identification.

Despite the efficacy of the JSWD model in refining image edges and details, it is acknowledged that the computational demands are substantial, necessitating advanced computational resources due to the combined regularization terms and the extensive iteration process. There remains ample scope for further inquiry. Key areas for future research include: Mitigating computational complexity to expedite processing speeds presents a formidable challenge; Reducing the number of iterations while ensuring the convergence of the JSWD algorithm is a compelling avenue for exploration; Considering the application of the algorithm on natural images with smooth gradients; Integrating optimization models with deep learning techniques to augment the deblurring capabilities for both grayscale and color images represents the cutting-edge trend in the field.

REFERENCES

[1] W. Dong, L. Zhang, G. Shi, and X. Wu, "Image deblurring and super-resolution by adaptive sparse domain selection and adaptive regularization," *IEEE Trans. Image Process.*, vol. 20, no. 7, pp. 1838–1857, Jul. 2011.

[2] S. Kindermann, S. Osher, and P. W. Jones, "Deblurring and denoising of images by nonlocal functionals," *Multiscale Model. Simul.*, vol. 4, no. 4, pp. 1091–1115, Jan. 2005.

[3] H. Takeda, S. Farsiu, and P. Milanfar, "Deblurring using regularized locally adaptive kernel regression," *IEEE Trans. Image Process.*, vol. 17, no. 4, pp. 550–563, Apr. 2008.

[4] A. Beck and M. Teboulle, "Fast gradient-based algorithms for constrained total variation image denoising and deblurring problems," *IEEE Trans. Image Process.*, vol. 18, no. 11, pp. 2419–2434, Nov. 2009.

[5] K. Dabov, A. Foi, V. Katkovnik, and K. Egiazarian, "BM3D image denoising with shape-adaptive principal component analysis," in *SPARS'09-Signal Processing With Adaptive Sparse Structured Representations*, 2009.

[6] G. Aubert and P. Kornprobst, *Mathematical Problems in Image Processing: Partial Differential Equations and the Calculus of Variations*. Cham, Switzerland: Springer, 2006.

[7] K. Dabov, A. Foi, V. Katkovnik, and K. Egiazarian, "Color image denoising via sparse 3D collaborative filtering with grouping constraint in luminance-chrominance space," in *Proc. IEEE Int. Conf. Image Process.*, Sep. 2007, pp. 1–19.

[8] M. Bergounioux and L. Piffet, "A second-order model for image denoising," *Set-Valued Variational Anal.*, vol. 18, nos. 3–4, pp. 277–306, Dec. 2010.

[9] K. Dabov, A. Foi, V. Katkovnik, and K. Egiazarian, "Image denoising by sparse 3-D transform-domain collaborative filtering," *IEEE Trans. Image Process.*, vol. 16, no. 8, pp. 2080–2095, Aug. 2007.

[10] J. F. Cai, R. Chan, and Z. W. Shen, "Image denoising by sparse 3-D transform-domain collaborative filtering," *Inverse Problems Imag.*, vol. 16, no. 8, pp. 2080–2095, Aug. 2017.

[11] B. Dong, H. Ji, J. Li, Z. Shen, and Y. Xu, "Wavelet frame based blind image inpainting," *Appl. Comput. Harmon. Anal.*, vol. 32, no. 2, pp. 268–279, Mar. 2012.

[12] M. A. T. Figueiredo, R. D. Nowak, and S. J. Wright, "Gradient projection for sparse reconstruction: Application to compressed sensing and other inverse problems," *IEEE J. Sel. Topics Signal Process.*, vol. 1, no. 4, pp. 586–597, Dec. 2007.

[13] W. Yin, S. Osher, D. Goldfarb, and J. Darbon, "Bregman iterative algorithms for ℓ_1-minimization with applications to compressed sensing," *SIAM J. Imag. Sci.*, vol. 1, no. 1, pp. 143–168, Jan. 2008.

[14] H. Xu, G. Zhai, and X. Yang, "Single image super-resolution with detail enhancement based on local fractal analysis of gradient," *IEEE Trans. Circuits Syst. Video Technol.*, vol. 23, no. 10, pp. 1740–1754, Oct. 2013.

[15] L. Wang, S. Xiang, G. Meng, H. Wu, and C. Pan, "Edge-directed single-image super-resolution via adaptive gradient magnitude self-interpolation," *IEEE Trans. Circuits Syst. Video Technol.*, vol. 23, no. 8, pp. 1289–1299, Aug. 2013.

[16] A. Chambolle and P.-L. Lions, "Image recovery via total variation minimization and related problems," *Numerische Math.*, vol. 76, no. 2, pp. 167–188, Apr. 1997.

[17] S. Li, B. Zhang, X. Yang, and W. Zhu, "Edge-guided second-order total generalized variation for Gaussian noise removal from depth map," *Sci. Rep.*, vol. 10, no. 1, pp. 1–24, Oct. 2020.

[18] J.-F. Cai, B. Dong, S. Osher, and Z. Shen, "Image restoration: Total variation, wavelet frames, and beyond," *J. Amer. Math. Soc.*, vol. 25, no. 4, pp. 1033–1089, Oct. 2012.

[19] D. Geman and G. Reynolds, "Constrained restoration and the recovery of discontinuities," *IEEE Trans. Pattern Anal. Mach. Intell.*, vol. 14, no. 3, pp. 367–383, Mar. 1992.
[20] D. Mumford and J. Shah, "Constrained restoration and the recovery of discontinuities," *Pattern Anal. Mach. Intell.*, vol. 42, pp. 557–685, May 1989.
[21] Y. Cui, W. Ren, X. Cao, and A. Knoll, "Image restoration via frequency selection," *IEEE Trans. Pattern Anal. Mach. Intell.*, vol. 46, no. 2, pp. 1093–1108, Feb. 2024.
[22] K. Zhang, W. Zuo, S. Gu, and L. Zhang, "Learning deep CNN denoiser prior for image restoration," in *Proc. IEEE Conf. Comput. Vis. Pattern Recognit. (CVPR)*, Jul. 2017, pp. 2808–2817.
[23] T. Wang, Y. Xiao, Y. Cai, G. Gao, X. Jin, L. Wang, and H. Lai, "UFSRNet: U-shaped face super-resolution reconstruction network based on wavelet transform," *Multimedia Tools Appl.*, vol. 83, no. 25, pp. 67231–67249, Jan. 2024.
[24] X. Deng, C. Gao, and M. Xu, "PIRNet: Privacy-preserving image restoration network via wavelet lifting," in *Proc. IEEE/CVF Int. Conf. Comput. Vis. (ICCV)*, Oct. 2023, pp. 22368–22377.
[25] L. Calatroni, A. Lanza, M. Pragliola, and F. Sgallari, "Adaptive parameter selection for weighted-TV image reconstruction problems," in *Proc. 9th Int. Conf. New Comput. Methods for Inverse Problems*, vol. 1, 2019, pp. 1–24.
[26] G. Peyré, S. Bougleux, and L. Cohen, "Non-local regularization of inverse problems," *Inverse Problems Imag.*, vol. 5, no. 2, pp. 511–530, 2011.
[27] J. Zhang, D. Zhao, R. Xiong, S. Ma, and W. Gao, "Image restoration using joint statistical modeling in a space-transform domain," *IEEE Trans. Circuits Syst. Video Technol.*, vol. 24, no. 6, pp. 915–928, Jun. 2014.
[28] M. Jung, X. Bresson, T. F. Chan, and L. A. Vese, "Nonlocal Mumford-Shah regularizers for color image restoration," *IEEE Trans. Image Process.*, vol. 20, no. 6, pp. 1583–1598, Jun. 2011.
[29] Q. Liu, C. Liu, C. Ling, L. Sun, S. Gao, and M. Lin, "Image restoration and reconstruction by non-convex total variation and shearlet regularizations," *J. Electron. Imag.*, vol. 31, no. 1, pp. 1–20, Feb. 2022.
[30] W. Lian and X. Liu, "Non-convex fractional-order TV model for impulse noise removal," *J. Comput. Appl. Math.*, vol. 417, Jan. 2023, Art. no. 114615.
[31] Q. Zhong, C. Wu, Q. Shu, and R. W. Liu, "Spatially adaptive total generalized variation-regularized image deblurring with impulse noise," *J. Electron. Imag.*, vol. 27, no. 5, p. 1, Sep. 2018.
[32] J. Kim and S. Ahmad, "On the preconditioning of the primal form of TFOV-based image deblurring model," *Sci. Rep.*, vol. 13, no. 1, pp. 1–26, Oct. 2023.
[33] M. Z. Shi, "A novel gradient ℓ_0 norm regularization image restoration method based on non-local total variation," in *Proc. Int. Conf. Commun. Signal Process., Syst.*, 2019, pp. 1–22.
[34] Y. Zhang, Y. Shi, L. Ma, J. Wu, L. Wang, and H. Hong, "Blind natural image deblurring with edge preservation based on L_0-regularized gradient prior," *Optik*, vol. 225, Jan. 2021, Art. no. 165735.
[35] B. A. Hassan and M. Aziz, "Computational experience with modified coefficients conjugate gradient for image restoration," *Eur. J. Pure Appl. Math.*, vol. 16, no. 2, pp. 975–982, Apr. 2023.
[36] Q. An, T. Liu, Z. Huang, and H. Zeng, "Learning wavelet-transform based sparsity knowledge for blind infrared images restoration in students' training in the wild," *Infr. Phys. Technol.*, vol. 119, Dec. 2021, Art. no. 103955.
[37] C. Z. Deng, S. Q. Wang, and H. Q. Cao, "Fourier-curvelet transform combined image restoration," *Acta Optica Sinica*, vol. 29, no. 8, pp. 2134–2136, 2009.
[38] Y. C. Jiang and J. Zhang, "An algorithm for image restoration based on tight wavelet frames," in *Proc. Int. Conf. Intell. Inf. Technol. Appl.*, 2010, pp. 1–20.
[39] J.-F. Cai, B. Dong, and Z. Shen, "Image restoration: A wavelet frame based model for piecewise smooth functions and beyond," *Appl. Comput. Harmon. Anal.*, vol. 41, no. 1, pp. 94–138, Jul. 2016.
[40] J. K. Choi, B. Dong, and X. Zhang, "An edge driven wavelet frame model for image restoration," *Appl. Comput. Harmon. Anal.*, vol. 48, no. 3, pp. 993–1029, May 2020.
[41] G. Q. Dong, "Research on image restoration models under a prior constraint regularization framework," *Liaoning Univ. Eng. Technol.*, vol. 48, no. 3, pp. 993–1029, 2020.
[42] J.-F. Cai, S. Osher, and Z. Shen, "Split Bregman methods and frame based image restoration," *Multiscale Model. Simul.*, vol. 8, no. 2, pp. 337–369, Jan. 2010.
[43] J. F. Cai, S. Osher, and Z. W. Shen, "Convergence of the linearized Bregman iteration for ℓ_1 norm minimization," *Math. Comput.*, vol. 268, pp. 8–52, May 2009.
[44] T. Goldstein and S. Osher, "The split Bregman method for L1-regularized problems," *SIAM J. Imag. Sci.*, vol. 2, no. 2, pp. 323–343, Jan. 2009.
[45] C. G. Rafael, E. W. Richard, and L. E. Steven, *Digital Image Processing Using MATLAB*, 2nd ed., New York, NY, USA: Publishing House of Electronics Industry, 2009.
[46] A. Tanchenko, "Visual-PSNR measure of image quality," *J. Vis. Commun. Image Represent.*, vol. 25, no. 5, pp. 874–878, Jul. 2014.
[47] T. Chai and R. R. Draxler, "Root mean square error (RMSE) or mean absolute error (MAE)," *Geoscientific Model Develop. Discuss.*, vol. 7, no. 1, pp. 1525–1534, 2014.
[48] D. Brunet, E. R. Vrscay, and Z. Wang, "On the mathematical properties of the structural similarity index," *IEEE Trans. Image Process.*, vol. 21, no. 4, pp. 1488–1499, Apr. 2012.
[49] Z. Wang and A. C. Bovik, "A universal image quality index," *IEEE Signal Process. Lett.*, vol. 9, no. 3, pp. 81–84, Mar. 2002.

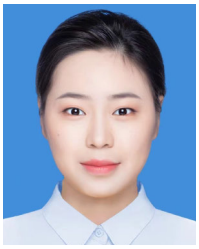

YONGQUN TAN was born in Chongqing, China, in 1997. She received the bachelor's degree in mathematics and applied mathematics from Chongqing University of Humanities and Technology, in 2021. She is currently pursuing the master's degree with Chongqing Jiaotong University. During her time in school, she received the National Inspirational Scholarship and passed the National English Test Band 4 and Band 6 and the National Computer Test Band 2, obtaining the Senior High School Teacher Qualification Certificate. Her research interest includes image restoration.

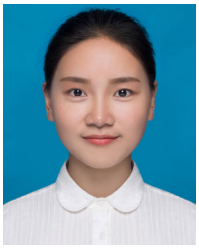

LINGLI ZHANG was born in Chongqing, China, in 1990. She received the B.S. degree in mathematics and applied mathematics and the Ph.D. degree in mathematics from Chongqing University, in 2011 and 2018, respectively.

From 2019 to 2022, she was a Lecturer with Chongqing Key Laboratory of Statistical Optimization and Complex Data and Chongqing Key Laboratory of Group and Graph Theories and Applications, Chongqing University of Arts and Sciences. Since 2023, she has been an Associate Professor with Chongqing Key Laboratory of Statistical Optimization and Complex Data and Chongqing Key Laboratory of Group and Graph Theories and Applications. She is currently working as a part-time Master's Mentor with Chongqing Jiaotong University, the Director of Chongqing Society of Industrial and Applied Mathematics, and the Commentator of mathematical review. She undertook ten national, provincial and ministerial projects, and one horizontal project. She has published more than ten papers.

YU CHEN was born in Anhui, China, in 2000. He received the bachelor's degree from the School of Mathematics and Statistics, Henan University. He is currently pursuing the degree with the School of Mathematics and Statistics, Chongqing Jiaotong University. His research interest includes image processing.